A New Approach to the Characteristics and Short-Channel Effects of Double-Gate Carbon Nanotube Field-Effect Transistors using MATLAB: A Numerical Study

Alireza Heidari, Niloofar Heidari, Foad Khademi Jahromi, Roozbeh Amiri, and Mohammadali Ghorbani

Institute for Advanced Studies, Tehran 14456-63543, Iran

Reprint requests to A. H.; E-mail: Prof.Alireza.Heidari@InstituteforAdvancedStudies.us

Z. Naturforsch. **67a,** 317 – 326 (2012) / DOI: 10.5560/ZNA.2012-0024
Received November 8, 2011

In this paper, first, the impact of different gate arrangements on the short-channel effects of carbon nanotube field-effect transistors with doped source and drain with the self-consistent solution of the three-dimensional Poisson equation and the Schrödinger equation with open boundary conditions, within the non-equilibrium Green function, is investigated. The results indicate that the double-gate structure possesses a quasi-ideal subthreshold oscillation and an acceptable decrease in the drain induced barrier even for a relatively thick gate oxide (5 nm). Afterward, the electrical characteristics of the double-gate carbon nanotube field-effect transistors (DG-CNTFET) are investigated. The results demonstrate that an increase in diameter and density of the nanotubes in the DG-CNTFET increases the on-state current. Also, as the drain voltage increases, the off-state current of the DG-CNTFET decreases. In addition, regarding the negative gate voltages, for a high drain voltage, increasing in the drain current due to band-to-band tunnelling requires a larger negative gate voltage, and for a low drain voltage, resonant states appear.

Key words: Short-Channel Effects; Non-Equilibrium Green Function; Field-Effect Transistor; Double-Gate; Carbon Nanotube.

1. Introduction

After the discovery of nanotubes by Iijima [1], in terms of physical and technological modelling, significant progresses have been accomplished in the field of carbon nanotube field-effect transistors (CNTFET). For instance, the empirical results of the CNTFET of the Schottky barrier are achieved [2] and illustrate that the current, mainly, is produced at the two ends of the nanotube by the induction field of the band structure of the nanotube. Certainly, such mechanism highly restricts the efficiency of the device. Pseudo-bipolar behaviour [3 – 8], weak channel control, the degradation of electrical characteristics such as the leakage-current increase, and subthreshold oscillations are observed in such devices, especially in the transistors consisting of nanotubes with larger diameters [9, 10]. It is also experimentally proved that in order to decrease the drain induced barrier (DIBL) to an acceptable value, reducing the transistor dimensions must follow specific rules [9] (for example, the ratio of the channel length to the oxide thickness must be more than 18).

Hereunto, various solutions to overcome these defects have been proposed of which the selecting palladium and calcium as contacts' substance to create Ohmic contacts [11, 12] and the method of producing induction charges [13, 14] can be mentioned. Additionally, the efficiency of the transistors can be increased through defining multiple gates, since, by means of it, the independent potential in the areas of source, drain, and channel can be produced, and the Schottky barrier in the contact can be created.

In this article, the impact of different gate structures on the short-channel effects of a CNTFET with doped source and drain is simulated three-dimensionally through using the MATLAB software. Since the results show that the double-gate structure of the CNTFET, which is plotted in Figure 1, has quasi-ideal subthreshold oscillations and an acceptable DIBL, the impact of different parameters on the short-channel effects and its electrical characteristics is investigated. The simulation is based on the solution of the Schrödinger equation with open boundary conditions, within the non-equilibrium Green's function (NEGF), and the

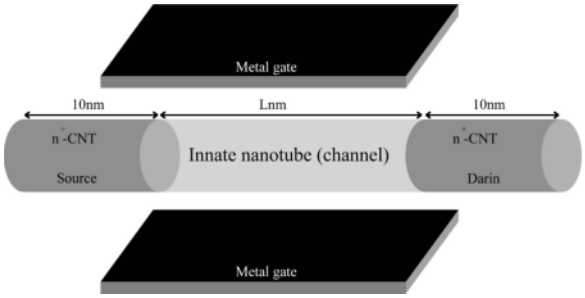

Fig. 1. Simulated three-dimensional structure of the DG-CNTFET.

method of moments [15] is employed to solve the three-dimensional Poisson equation.

2. Simulation Method

2.1. Transfer Equation with NEGF Method

The Green's function is defined as follows [16]:

$$G(E) = [EI - H - \Sigma_S - \Sigma_D]^{-1}, \tag{1}$$

where E is the energy, I the unit matrix, H the Hamiltonian matrix of the nanotube, Σ_S and Σ_D are the self-energy matrices of the source and drain, respectively. If the total number of carbon atoms of the nanotube is N, the size of the Hamiltonian matrix will be $N \times N$. As (1) indicates, without regard to the term of Σ_{scat}, which is related to the scattering of electrons, the completely ballistic transfer for simulating the transistors' behaviour is considered.

The entire arrays of the source's self-energy matrix Σ_S equal zero except for the array $(1,1)$ which is defined as follows:

$$\Sigma_S(1,1) = \frac{(E-U_1)^2 + t^2 + b_{2m}^2}{2(E-U_1)} \pm \frac{\sqrt{\left[(E-U_1)^2 + t^2 + b_{2m}^2\right]^2 - 4(E-U_1)^2 t^2}}{2(E-U_1)}, \tag{2}$$

where E is the energy, U_1 denotes the potential matrix's array $(1,1)$, $t \approx 3$ eV represents the interaction potential of two adjacent lattice sites in tight-binding model, and $b_{2m} = 2t\cos(\pi m/n)$, where n is related to the chirality of the nanotube, and m is the angular-momentum quantum number which gets the right values.

Similarly, the array (N,N) is the only non-zero array of the self-energy matrix of the drain, which is similar to (2) except that instead of U_1, U_N, the array (N,N) of the potential matrix is positioned.

The current is calculated as follows:

$$I = \frac{2q}{h}\int_{-\infty}^{+\infty} \mathrm{d}E\, T(E)\left[f(E-E_{FS}) - f(E-E_{FD})\right], \tag{3}$$

where q is the electron charge, h the Planck constant, and $T(E)$ the transfer coefficient which is computed as [17]

$$T = -\mathrm{Tr}\left[\left(\Sigma_S - \Sigma_S^{\dagger}\right) G \left(\Sigma_D - \Sigma_D^{\dagger}\right) G^{\dagger}\right], \tag{4}$$

where Tr is trace operator. Definitely, through this model, the one-dimensional transfer between source and drain can solely be simulated; that means that the gate-leakage current is not considered in this model, since it can be shown that for transistors with channel length of a few nanometers, the gate current is negligible in comparison to the drain current.

In numerical terms, the Green function is computed through the recursive technique [18, 19]. It should be noted here that in most simulations, for semi-finite contacts, the self-energy matrix is written as a boundary condition. Consequently, it can be considered that the ends of the nanotube are attached to two long infinite nanotubes.

3. Poisson Equation

In order to simulate the device through using the finite element method, the discretization is performed first in space, and then the transfer equations for the whole space volume elements are calculated separately. To achieve the diagonal elements of the Hamiltonian matrix H in (1), which is the electrostatic potential of each carbon atom's position, the Poisson equation must be used. In three-dimensional simulations, the Poisson equation is computed as follows:

$$\nabla\left[\varepsilon(\vec{r})\nabla U(\vec{r})\right] = p(\vec{r}) - n(\vec{r}) + N_D^+(\vec{r}) - N_A^-(\vec{r}) + \rho_{fix}, \tag{5}$$

where $U(\vec{r})$ is the electrostatic potential, $\varepsilon(\vec{r})$ the dielectric constant, $N_D^+(\vec{r})$, $N_A^-(\vec{r})$, and ρ_{fix} are, respectively, donor ion density, receptor ion density, and constant charge density. The constant charge density is considered zero, and the density of the electrons and holes (n and p, respectively) with the solution of the Schrödinger equation with open boundary conditions is calculated through the formulation

of non-equilibrium Green's function (NEGF) [20]. In addition, to solve the Schrödinger equation, the tight-binding Hamiltonian in the actual spatial atomic base (the orbitals of p_z) is utilized [21]. The advantage that actual spatial bases possess over modal spatial bases is a result of considering the current due to the middle-band and internal-band tunnelling phenomena. The reason of this matter is that the whole nanotube's bands are considered simultaneously in the method of actual spatial bases.

In this article, zigzag nanotubes are used; however, the method proposed in this paper can be generalized to nanotubes with any type of chirality, since the amendments only in the Hamiltonian matrix are required. Hence, first, the length and chirality of the nanotube are defined. Next, the three-dimensional coordinates of each carbon atom is calculated [21]. Thereafter, the three-dimensional range of simulation is determined and the lattice points are defined in accordance with each carbon atom. Furthermore, through the approximation of point charge, the entire free charges around each carbon atom can be distributed uniformly in the unit cell containing each atom. Assuming that the chemical potential of source and drain, in the equilibrium state, equal the Fermi level of the nanotube, the electron density is given as

$$n(\vec{r}) = 2\int_{E_i}^{+\infty} \mathrm{d}E\left[\left|\psi_{\mathrm{S}}(E,\vec{r})\right|^2 f(E-E_{\mathrm{FS}}) + \left|\psi_{\mathrm{D}}(E,\vec{r})\right|^2 f(E-E_{\mathrm{FD}})\right]. \tag{6}$$

Moreover, the hole density is

$$p(\vec{r}) = 2\int_{-\infty}^{E_i} \mathrm{d}E\left[\left|\psi_{\mathrm{S}}(E,\vec{r})\right|^2 (1-f(E-E_{\mathrm{FS}})) + \left|\psi_{\mathrm{D}}(E,\vec{r})\right|^2 (1-f(E-E_{\mathrm{FD}}))\right], \tag{7}$$

where $\vec{r}$ is the coordinate of each carbon atom, f the Fermi-Dirac distribution function, $|\psi_{\mathrm{S}}|^2$ ($|\psi_{\mathrm{D}}|^2$) is the probability of filling the atomic states of the carbon atom by the source (drain) vehicles, E_{FS} (E_{FD}) is the Fermi level of the source (drain), and E_i is the middle-band energy of the nanotube; in other words, the charge neutrality level [22, 23].

On account of computing this new U by the Poisson equation, the Hamiltonian H and the transfer equation NEGF (1) should be calculated again. That means that a self-consistent ring occurs between the Poisson equation and the quantum transport equation, and this ring resumes until the convergence is achieved which means that the maximum change in potential is lesser than the specified error value $(\max|U^{\mathrm{new}} - U^{\mathrm{previous}}|) \leq U^{\mathrm{tol}}$. The value of the potential tolerance U^{tol} is generally considered as 1 meV.

In numerical terms, a nonlinear system is solved by virtue of the Newton–Raphson method with the Gummel plot. The Schrödinger equation is solved in the beginning of each Newton–Raphson ring of the Poisson equation, and the charge density of the nanotube is assumed constant until the Newton ring becomes convergent. The cycle of algorithm resumes until the computed potential difference at the end of two Newton rings becomes less than 1 meV.

In the use of the recursive technique, since the electron density in each Newton ring is independent of the potential, the Jacobian is zero in the points of the range containing carbon atoms, and the control of the correction of the potential disappears and the convergence problem occurs. Therefore, to address the convergence problem, a method of conjecturing the value of charge is employed to achieve the approximate value of the Jacobian in each Newton ring. For this purpose, an exponential function is used to speculate on the value of charge [24], in this case, if n is the electron density, similar to (5), the density of electrons in the ith stage of Newton ring. n_i is expressed as follows:

$$n_i = n\,\mathrm{e}^{\left(\frac{\varphi_i - \tilde{\varphi}}{V_{\mathrm{T}}}\right)}, \tag{8}$$

where $\tilde{\varphi}$ and φ_i are, respectively, the computed electrostatic potential in the first and the ith stage of the Newton ring, and V_{T} is the thermal voltage. The same computational process is considered for the density of holes.

4. Results and Discussion

In this paper, a zigzag nanotube (11, 0) with a diameter of 0.9 nm, embedded in SiO_2 [25], is used. In addition, the intrinsic nanotube (non-doped) with the variable length L operates as the channel, and at its ends, the doped nanotube with n-type atoms and a length of 10 nm operates as the source and drain. It should be noted that in the source and drain of these transistors, there are approximately f donor atoms per carbon atom.

To consider the efficiency of the CNTFET transistors, first, their direct current (DC) characteristics are investigated. Afterwards, the transistors' behaviour is

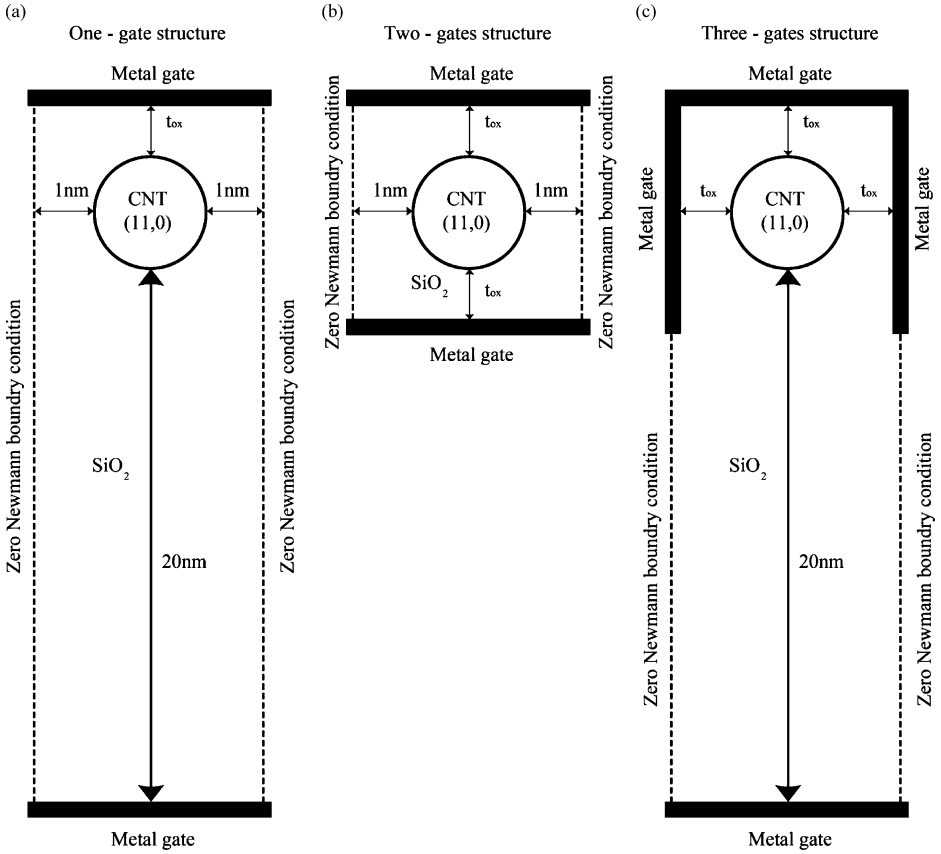

Fig. 2. Transverse cross section of the carbon nanotube field-effect transistor, (a) single-gate, (b) double-gate, and (c) triple-gate. The Neumann boundary conditions in the lateral faces of the transverse cross section are assumed zero.

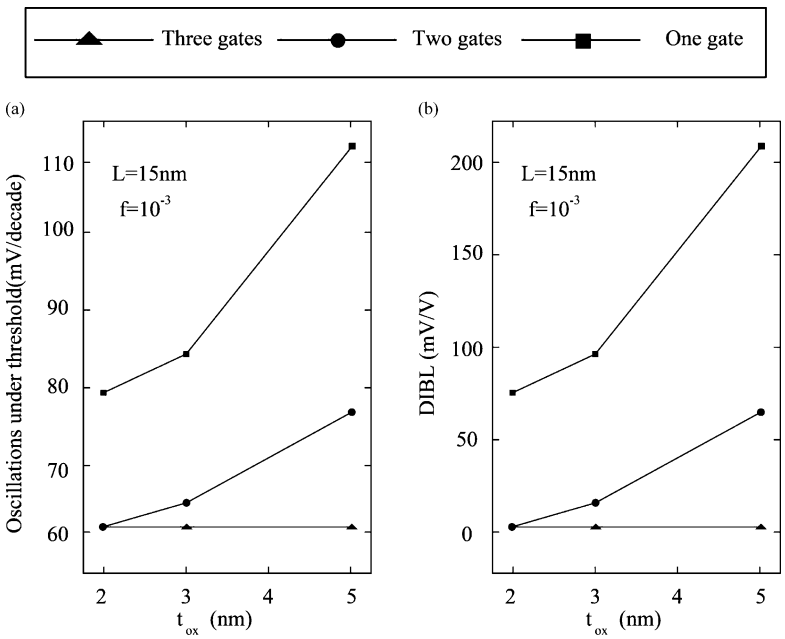

Fig. 3. (a) Subthreshold oscillations, (b) DIBL as a function of gate oxide related to the different gate arrangements.

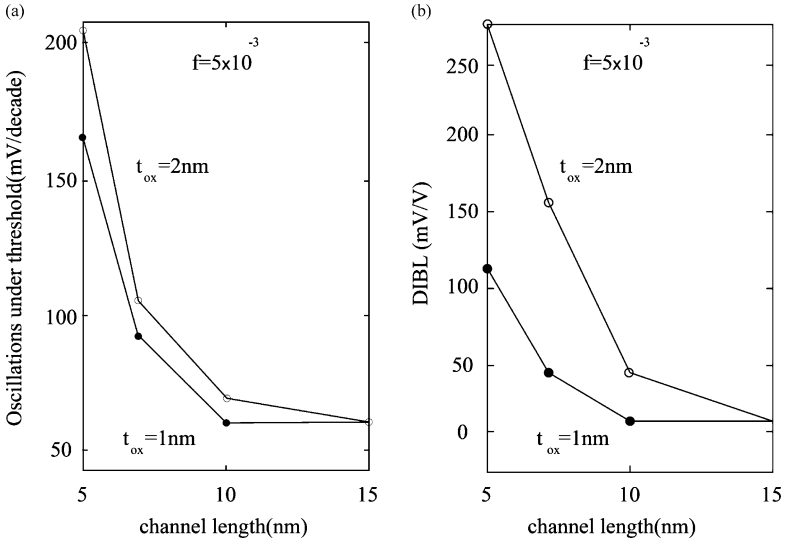

Fig. 4. (a) Subthreshold oscillations, (b) DIBL according to the channel length of the DG-CNTFET with a oxide thickness of 1 and 2 nm.

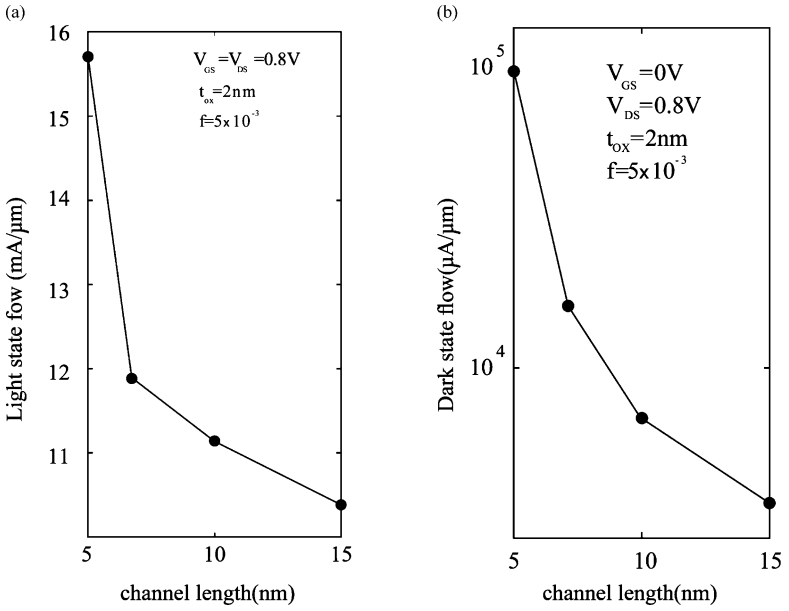

Fig. 5. (a) On-state current (I_{on}) and (b) off-state current (I_{off}) per length unit according to the channel length of the DG-CNTFET.

analyzed according to the short-channel effects, I_{on} and I_{off} currents. Furthermore, the short-channel effects for the different gate arrangements (single-gate, double-gate, and triple-gate) with the constant length of 15 nm are investigated in Figure 2. In order to apply an array of nanotubes, the Neumann boundary conditions in the lateral faces of the transverse cross section are used. The subthreshold oscillations and DIBL as a function of gate oxide are plotted in Figure 2a and 2b, respectively. As expected, the more the gate surrounds the channel, the better is the control over the channel. Consequently, the triple-gate transistor shows an ideal behaviour even for the thickest considered gate oxide (5 nm).

Moreover, in Figure 3, it can be seen that the double-gate structure indicates acceptable quasi-ideal subthreshold oscillations and the DIBL in the considered thickness range of SiO_2. However, the single-gate transistor demonstrates solely acceptable subthreshold oscillations and DIBL for the thin gate oxide (2 nm).

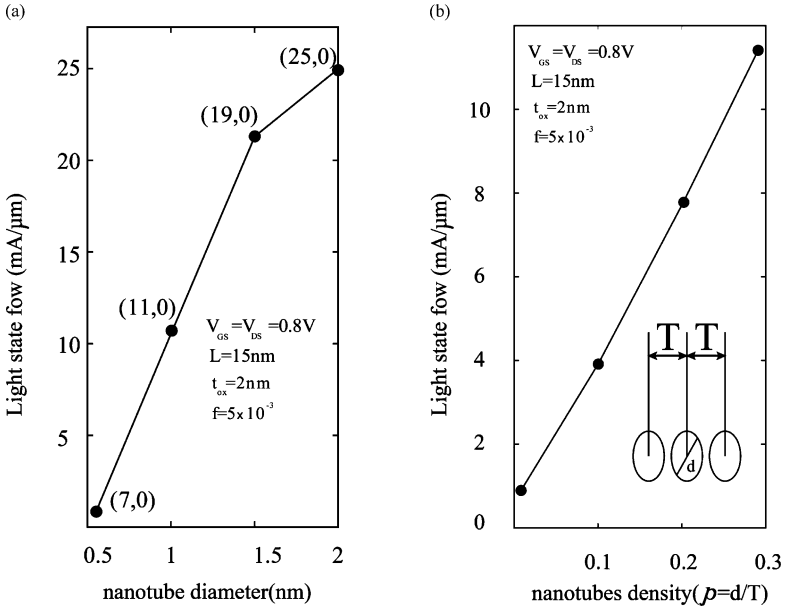

Fig. 6. (a) On-state current according to the diameter of the nanotube, (b) on-state current according to the density of the nanotube (the number of nanotubes in a length unit, $\rho = d/T$, as can be seen in the additional section of the figure; T is the distance between the centers of two nanotubes). The on-state current (I_{on}) in $V_{DS} = V_{GS} = 0.8$ V has been calculated.

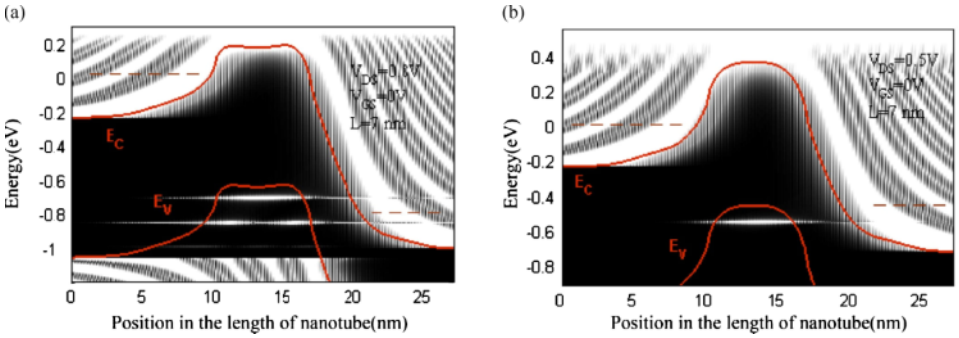

Fig. 7 (colour online). Density of nanotube states in the DG-CNTFET according to the energy and coordinates of the nanotube for $V_{GS} = 0$ V and (a) $V_{DS} = 0.8$ V (b) $V_{DS} = 0.5$ V. The dashed lines indicate the Fermi level of source and drain.

Now, we consider the characteristics of the double-gate carbon nanotube field-effect transistor (DG-CNTFET), which is plotted in Figure 1, and its cross section, which is illustrated in Figure 2b. The sub-threshold oscillations and DIBL of this transistor are plotted in Figure 4a and 4b, respectively, according to a function of the channel length of the DG-CNTFET with the oxide thickness of 1 and 2 nm. As these figures demonstrate, for the channel length of 10 nm, the DG-CNTFET shows its excellent performance. Figure 5a and 5b indicate respectively the on-state current (I_{on}) and off-state current (I_{off}) per unit length according to the channel length in the DG-CNTFET. When the length of the channel is reduced, the short-channel effects become more significant, and in the identical biasing conditions, the transistor with a shorter length indicates more current owing to the reduction in the channel barrier. It should be noted that the I_{on} current in $V_{DS} = V_{GS} = 0.8$ V and the I_{off} current in $V_{GS} = 0$ V, $V_{DS} = 0.8$ V are calculated.

The I_{on} is plotted in Figure 6a as a function of the nanotube diameter with a channel length of 7 nm. When the diameter of the nanotube increases, the quantized energy levels of each atom of the nanotube ring approach to each other, consequently; more subbands are involved in the electron transfer and the channel

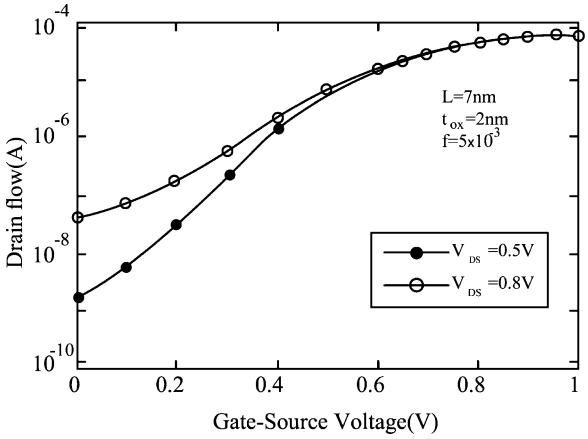

Fig. 8. Transfer characteristic of the DG-CNTFET with a channel length of 7 nm and an oxide thickness of 2 nm, for $V_{DS} = 0.5$ V and $V_{DS} = 0.8$ V.

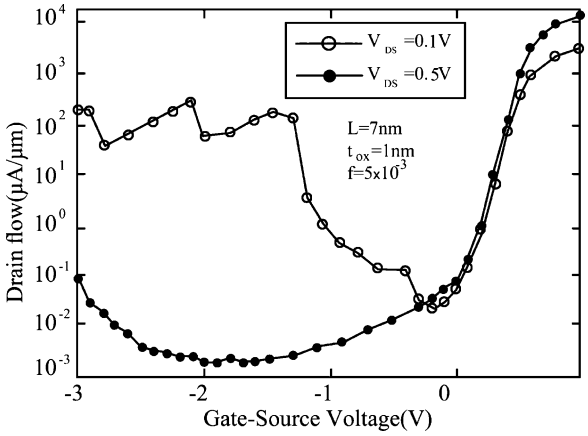

Fig. 9. Transfer characteristic of the DG-CNTFET with a channel length of 7 nm and an oxide thickness of 1 nm, for $V_{DS} = 0.1$ V and $V_{DS} = 0.5$ V.

conduction increases. Figure 6b illustrates the I_{on} according to the density of the nanotube (the number of nanotubes in a length unit, $\rho = d/T$, as can be seen in the additional section of Figure 6b; T is the distance between the centers of two nanotubes). Based on this figure, by increasing the density of the carbon nanotubes, the current also increases.

Another interesting point about the DG-CNTFET is that the increase in the I_{off} current is accompanied by an increase in the voltage of drain, since increasing the voltage of drain–source, the holes which are tunnelling from drain to source occupy the bound states existing in the shell capacity (Fig. 7a). However, for lower voltages of drain (Fig. 7b), the bound states are far distant from the Fermi level; therefore, as can be seen in Figure 8, the linear behaviour in the subthreshold region for the semi-logarithmic transfer characteristic curve is achieved. It should be noted that in the entire simulation, the Fermi level of the source is remained constant in zero energy.

Another impact of the bound states on the characteristic of the DG-CNTFET appears in negative gate voltages. Since the band-to-band tunnelling occurs in both the drain and source, the current in negative gate voltages also increases. Hence, as can be seen in Figure 9, for higher drain voltages, the increase in drain current requires a greater negative gate voltage, since, in high drain voltage, the impact of the bound states on the capacity band intensifies. Consequently, the probability of band-to-band tunnelling reduces. Additionally, it is observed in Figure 9 that in $V_{DS} = 0.1$ V, the resonant states appear in negative gate voltages.

5. Conclusion

In this paper, the electrical characteristics and the short-channel effects of the carbon nanotube field-effect transistor with doped drain and source are investigated through using a three-dimensional simulation and according to the non-equilibrium Green's function. Furthermore, the impact of different gate arrangements and changing the transistor dimensions are analyzed. The results indicate that the double-gate structure possesses acceptable subthreshold oscillations and DIBL in different channel lengths, and increasing the diameter and density of the nanotube, its on-state current also increases. In addition, the leakage current of the DG-CNTFET increases by the increase in the drain–source voltage. The important result which should be mentioned is that in negative gate voltages and high drain voltage, the increase in drain current due to band-to-band tunnelling requires a higher negative gate voltage, and the resonant states appear in negative gate voltages and low drain voltage.

Acknowledgement

The work described in this paper was fully supported by grants from the Institute for Advanced Studies of Iran. The authors would like to express genuinely and sincerely thanks and appreciated and their gratitude to the Institute for Advanced Studies of Iran.

Appendix A

Let us consider a coaxial gate geometry, with the carbon nanotube as a one-dimensional object (radius zero), located at the axis of the structure ($r=0$). In the quantum capacitance limit, the charge in the nanotube is zero, and the electrostatics of his system is governed by Laplace's equation:

$$\frac{1}{r}\frac{\partial}{\partial r}\left(r\frac{\partial E(r,z)}{\partial r}\right)+\frac{\partial^2 E(r,z)}{\partial z^2}=0\,, \tag{A.1}$$

where $E(r,z)$ is the potential energy. We will assume that in the radial direction the potential energy is of parabolic type:

$$E(r,z)=a(z)\,r^2+b(z) \tag{A.2}$$

with $a(z)$ and $b(z)$ z-dependent functions. The linear term in r was not included because of symmetry considerations. The boundary condition at the surface of the cylindrical structure is $E(r=t_{\rm ox},z)=\phi_{\rm SB}-(V_{\rm GS}-V_{\rm FB})$. Replacing (A.2) into (A.1), we can write the following effective one-dimensional Laplace equation at the cylinder axis ($r=0$):

$$\frac{{\rm d}^2 a(z)}{{\rm d}z^2}-\frac{a(z)}{\lambda^2}=0 \tag{A.3}$$

with $\lambda=t_{\rm ox}/2$ a characteristic length that can be interpreted as a measure of the Schottky barrier width. (A.3) has the general solution $a(z)=A\exp(-z/\lambda)+B\exp(z/\lambda)$. For determining A and B, the following two boundary conditions must be satisfied:

$$\begin{aligned}&E(r=0,z=0)=\phi_{\rm SB}\,,\\&E(r=0,z=\infty)=\phi_{\rm SB}-(V_{\rm GS}-V_{\rm FB})\,,\end{aligned} \tag{A.4}$$

yielding the potential energy profile along the center of the system as

$$\begin{aligned}&E(r=0,z)=E(z)-\phi_{\rm SB}\\&-(V_{\rm GS}-V_{\rm FB})\,(1-\exp(-z/\lambda))\,.\end{aligned} \tag{A.5}$$

Appendix B

In this appendix, the Green functions are computed, assuming a Luttinger liquid with a homogeneous interaction parameter $K_{j\delta}$ and velocity $v_{j\delta}$. The product $v_{j\delta}K_{j\delta}$ corresponds to the Fermi velocity $v_{\rm F}$.

The finite temperature action associated with this problem has the general form

$$\begin{aligned}S=\frac{1}{2}\sum_{j\delta}\int_0^\beta {\rm d}\tau\int_{-\infty}^{\infty}{\rm d}x\Big(&v_{j\delta}K_{j\delta}(\partial_x\varphi_{j\delta}(x,\tau))^2\\&+\frac{v_{j\delta}}{K_{j\delta}}(\partial_x\theta_{j\delta}(x,\tau))^2\\&+2{\rm i}(\partial_x\varphi_{j\delta}(x,\tau))(\partial_\tau\theta_{j\delta}(x,\tau))\Big)\,,\end{aligned} \tag{B.1}$$

which implies that the Fourier transform of the time ordered Green functions $G^{\theta\theta}_{j\delta(T)}$ and $G^{\varphi\varphi}_{j\delta(T)}$, defined as

$$\begin{aligned}G^{\theta\theta}_{j\delta(T)}(x,x',t)=&\langle T\theta_{j\delta}(x,t)\theta_{j\delta}(x',0)\rangle\\&-\langle T\theta^2_{j\delta}(x,t)\rangle\,,\end{aligned} \tag{B.2}$$

$$\begin{aligned}G^{\varphi\varphi}_{j\delta(T)}(x,x',t)=&\langle T\varphi_{j\delta}(x,t)\varphi_{j\delta}(x',0)\rangle\\&-\langle T\varphi^2_{j\delta}(x,t)\rangle\,,\end{aligned} \tag{B.3}$$

where T is the time ordered operator, satisfies the differential equations

$$\begin{aligned}&\left(\frac{\omega^2}{v_{j\delta}K_{j\delta}}-\partial_x\frac{v_{j\delta}}{K_{j\delta}}\partial_x\right)G^{\theta\theta}_{j\delta(T)}(x,x',\omega)\\&=4\pi\delta(x-x')\,,\end{aligned} \tag{B.4}$$

$$\begin{aligned}&\left(-\frac{K_{j\delta}\omega^2}{v_{j\delta}}+\partial_x v_{j\delta}K_{j\delta}\partial_x\right)G^{\varphi\varphi}_{j\delta(T)}(x,x',\omega)\\&=4\pi\delta(x-x')\,.\end{aligned} \tag{B.5}$$

The Green function $G^{\theta\theta}_{j\delta(T)}$ is continuous everywhere, and $v_{j\delta}[\partial_x G^{\theta\theta}_{j\delta(T)}]/K_{j\delta}$ has a discontinuity at $x=x'$. The similarity between (B.4) and (B.5) results from the duality properties of the underlying fields. All information on $G^{\varphi\varphi}_{j\delta(T)}$ is obtained by dividing $G^{\theta\theta}_{j\delta(T)}$ by $K^2_{j\delta}$.

There are additional Green functions in our problem which involve the fields θ and φ. For instance

$$\begin{aligned}G^{\varphi\theta}_{j\delta(T)}(x,x',t)=&\left\langle T\varphi_{j\delta}(x,t)\theta_{j\delta}(x',0)\right\rangle\\&-\left\langle T\varphi_{j\delta}(x,t)\theta_{j\delta}(x,t)\right\rangle\,.\end{aligned} \tag{B.6}$$

Using the action (B.1), one can show that (t is a real time variable)

$$\begin{aligned}&\left\langle\partial_x\varphi_{j\delta}(x,t)\theta_{j\delta}(x',0)\right\rangle\\&=\frac{1}{v_{j\delta}K_{j\delta}}\left\langle\partial_t\theta_{j\delta}(x,t)\theta_{j\delta}(x',0)\right\rangle\end{aligned} \tag{B.7}$$

and similarly for $G^{\theta\varphi}_{j\delta(T)}$.

From these real time Green functions, we further specify the Keldysh matrix elements which two times, t and 0, are assigned to the upper/lower branch $(++,+-,-+,--)$. Given an arbitrary real time Green function $G(x,x',t) = \langle A(x,t)B(x',0)\rangle - \langle A(x,t)B(x,t)\rangle$, a general procedure for obtaining these elements is as follows:

$$G^{\theta\theta}_{j\delta(K)}(x,x',t) = \begin{pmatrix} G^{\theta\theta}_{j\delta}(x,x',|t|) & G^{\theta\theta}_{j\delta}(x',x,-t) \\ G^{\theta\theta}_{j\delta}(x,x',t) & G^{\theta\theta}_{j\delta}(x',x,-|t|) \end{pmatrix}, \tag{B.8}$$

where

$$G^{\theta\theta}_{j\delta}(x,x',t) = -\frac{K_{j\delta}}{8\pi}\sum_r \ln\left(1+\mathrm{i}\frac{v_\mathrm{F}t}{a}+\mathrm{i}r\frac{K_{j\delta}(x-x')}{a}\right). \tag{B.9}$$

The same applies to $G^{\varphi\varphi}_{j\delta(K)}$ for which we have

$$G^{\theta\theta}_{j\delta}(x,x',t) = -\frac{1}{8\pi K_{j\delta}}\sum_r \ln\left(1+\mathrm{i}\frac{v_\mathrm{F}t}{a}+\mathrm{i}r\frac{K_{j\delta}(x-x')}{a}\right). \tag{B.10}$$

The mixed correlators read

$$G^{\varphi\theta}_{j\delta(K)}(x,x',t) = \begin{pmatrix} t>0: G^{\varphi\theta}_{j\delta}(x,x',t) & G^{\theta\varphi}_{j\delta}(x',x,-t) \\ t<0: G^{\theta\varphi}_{j\delta}(x',x,-t) & t>0: G^{\theta\varphi}_{j\delta}(x',x,-t) \\ G^{\varphi\theta}_{j\delta}(x,x',t) & t<0: G^{\varphi\theta}_{j\delta}(x,x',t) \end{pmatrix}, \tag{B.11}$$

where

$$G^{\theta\varphi}_{j\delta}(x,x',t) = -\frac{1}{8\pi}\sum_r r\ln\left(1+\mathrm{i}\frac{v_\mathrm{F}t}{a}+\mathrm{i}r\frac{K_{j\delta}(x-x')}{a}\right). \tag{B.12}$$

The same applies to $G^{\theta\varphi}_{j\delta(K)}$ for which we have

$$G^{\varphi\theta}_{j\delta}(x,x',t) = -\frac{1}{8\pi}\sum_r r\ln\left(1+\mathrm{i}\frac{v_\mathrm{F}t}{a}+\mathrm{i}r\frac{K_{j\delta}(x-x')}{a}\right). \tag{B.13}$$

Appendix C

We now compute the integrals involved in the tunnelling current and noise. The general integrals which will be required to compute the current and noise read

$$\int_{-\infty}^{+\infty}\frac{\sin(\omega_0\tau)\,\mathrm{d}\tau}{\left(\frac{a}{u^\sigma_\mathrm{F}}-\mathrm{i}\eta\tau\right)\left(\frac{a}{v_\mathrm{F}}-\mathrm{i}\eta\tau\right)^\nu} \approx \mathrm{i}\pi\eta\,\mathrm{sgn}(\omega_0)\frac{|\omega_0|^\nu}{\Gamma(\nu+1)}, \tag{C.1}$$

$$\int_{-\infty}^{+\infty}\frac{\cos(\omega_0\tau)\,\mathrm{d}\tau}{\left(\frac{a}{u^\sigma_\mathrm{F}}-\mathrm{i}\eta\tau\right)\left(\frac{a}{v_\mathrm{F}}-\mathrm{i}\eta\tau\right)^\nu} \approx \pi\,\mathrm{sgn}(\omega_0)\frac{|\omega_0|^\nu}{\Gamma(\nu+1)}. \tag{C.2}$$

We now write the integral which appears in the nanotube current, which refer to the propagation along the nanotube:

$$I_2 = \int_{-\infty}^{+\infty}\mathrm{d}\tau'\partial_x\big(G^{\varphi\varphi}_{c+(++)}(x,0,\tau') - G^{\varphi\varphi}_{c+(--)}(x,0,\tau') + G^{\varphi\varphi}_{c+(-+)}(x,0,\tau') - G^{\varphi\varphi}_{c+(+-)}(x,0,\tau')\big). \tag{C.3}$$

Using the expressions for the Green functions (Appendix B), we have

$$I_2 = \frac{\mathrm{i}}{\pi v_\mathrm{F}}\arctan\left(\frac{K_{j\delta}x}{a}\right) \approx \mathrm{i}\frac{\mathrm{sgn}(x)}{2v_\mathrm{F}}, \tag{C.4}$$

where the approximate sign holds at large distances.

The integrals which are involved for the computation of the noise are

$$I^{\varphi\varphi}(x,x') = 4I_3(x)I_3(x'), \tag{C.5}$$

$$I^{\varphi\theta}(x,x') = 4I_4(x)I_4(x') \tag{C.6}$$

with

$$I_3(x) = \int_{-\infty}^{+\infty}\mathrm{d}\tau\partial_x\big(G^{\varphi\varphi}_{c+(++)}(x,0,\tau) - G^{\varphi\varphi}_{c+(+-)}(x,0,\tau)\big) \approx \mathrm{i}\,\mathrm{sgn}(x)/4v_\mathrm{F}, \tag{C.7}$$

$$I_4(x) = \int_{-\infty}^{+\infty}\mathrm{d}\tau\partial_x\big(G^{\varphi\theta}_{c+(++)}(x,0,\tau) - G^{\varphi\theta}_{c+(+-)}(x,0,\tau)\big) \approx -\mathrm{i}K_{c+}/4v_\mathrm{F}. \tag{C.8}$$

[1] S. Iijima, Nature **354**, 56 (1991).
[2] S. Heinze, J. Tersoff, R. Martel, V. Derycke, J. Appenzeller, and P. Avouris, Phys. Rev. Lett. **89**, 106801 (2002).
[3] D. L. Pulfrey and L. Chen, Solid State Electron. **52**, 1324 (2008).
[4] M. Burghard, Surf. Sci. Rep. **58**, 1 (2005).
[5] P. G. Collins and P. Avouris, Contemp. Concepts Condensed Matter Sci. **3**, 49 (2008).
[6] I. Capek, Adv. Colloid Interface **150**, 63 (2009).
[7] B. S. Harrison and A. Atala, Biomaterials **28**, 344 (2007).
[8] A. Maiti, Microelectronics J. **39**, 208 (2008).
[9] J. Appenzeller, J. Knoch, R. Martel, V. Derycke, S. Wind, and P. Avouris, IEDM Tech. Dig. 285 (2002).
[10] C. Sandow, J. Knoch, C. Urban, Q.-T. Zhao, and S. Mantl, Solid State Electron. **53**, 1126 (2009).
[11] A. Javey, J. Guo, Q. Wang, M. Lundstrom, and H. Dai, Nature **424**, 654 (2003).
[12] Y. Nosho, Y. Ohno, S. Kishimoto, and T. Mizutani, Appl. Phys. Lett. **86**, 073105 (2005).
[13] J. Chen, C. Klinke, A. Afzali, and P. Avouris, Appl. Phys. Lett. **86**, 123108 (2005).
[14] M. Bockrath, J. Hone, A. Zettl, P. McEuen, A. G. Rinzler, and R. E. Smalley, Phys. Rev. B. Condens. Matter **61**, R10607 (2000).
[15] J. Guo, S. Datta, M. Lundstrom, and M. P. Anantram, Int. J. Multiscale Com. **2**, 257 (2004).
[16] S. Datta, Electronic Transport in Mesoscopic Systems, Cambridge University Press, New York 1995.
[17] S. Datta, Superlattices Microst. **28**, 253 (2000).
[18] R. Lake, G. Klimeck, R. C. Bowen, and D. Jovanovic, J. Appl. Phys. **81**, 7845 (1997).
[19] A. Svizhenko, M. P. Anantram, T. R. Govindam, and B. Biegel, J. Appl. Phys. **91**, 2343 (2001).
[20] J. Guo, A. Javey, D. Hongjai, and M. Lundstrom, IEDM Tech. Dig. 703 (2004).
[21] R. Saito, G. Dresselhaus, and M. S. Dresselhaus, Physical Properties of Carbon Nanotubes, Imperial College Press, London, U.K. 2003.
[22] J. Tersoff, Phy. Rev. Lett. **52**, 465 (1984).
[23] J. Tersoff, Phy. Rev. Lett. **56**, 675 (1986).
[24] M. P. Lopez Sancho, J. M. Lopez Sancho, and J. Rubio, J. Phys. F. Met. Phys. **15**, 851 (1984).
[25] A. G. Mamalis, L. O. G. Vogtländer, and A. Markopoulos, Precis. Eng. **28**, 16 (2004).